Journal Pre-proof

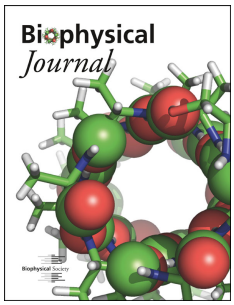

Integrin-Based Mechanosensing through Conformational Deformation

Tristan P. Driscoll, Tamara C. Bidone, Sang Joon Ahn, Alvin Yu, Alexander Groisman, Gregory A. Voth, Martin A. Schwartz

PII: S0006-3495(21)00744-X

DOI: https://doi.org/10.1016/j.bpj.2021.09.010

Reference: BPJ 11290

To appear in: *Biophysical Journal*

Received Date: 3 June 2021

Accepted Date: 7 September 2021

Please cite this article as: Driscoll TP, Bidone TC, Ahn SJ, Yu A, Groisman A, Voth GA, Schwartz MA, Integrin-Based Mechanosensing through Conformational Deformation, *Biophysical Journal* (2021), doi: https://doi.org/10.1016/j.bpj.2021.09.010.

Integrin-Based Mechanosensing through Conformational Deformation

Tristan P. Driscoll [1#*], Tamara C. Bidone[2,3#*], Sang Joon Ahn[4], Alvin Yu[6], Alexander Groisman[5], Gregory A. Voth[6] and Martin A. Schwartz[4,7,8]

[1]Department of Chemical and Biomedical Engineering, FAMU-FSU College of Engineering, Tallahassee, FL 32310

[2]Department of Biomedical Engineering, University of Utah, Salt Lake City, UT, 84102

[3]Scientific Computing and Imaging Institute, University of Utah, Salt Lake City, UT, 84102

[4]Yale Cardiovascular Research Center, Department of Cardiovascular Medicine, Yale University, New Haven, CT 06511

[5]Department of Physics, University of California San Diego

[6]Department of Chemistry, Chicago Center for Theoretical Chemistry, Institute for Biophysical Dynamics, and James Franck Institute, The University of Chicago, Chicago, IL 60637

[7]Department of Cell Biology, Yale University, New Haven, CT 06511

[8]Department of Biomedical Engineering, School of Engineering and Applied Science, Yale University, New Haven, CT 06511

*** Corresponding authors**: Tristan Driscoll (tdriscoll2@eng.famu.fsu.edu) and Tamara Bidone (tamarabidone@sci.utah.edu)

 # These authors contributed equally to this work

Date: 9/9/21

Abstract

Conversion of integrins from low to high affinity states, termed activation, is important in biological processes including immunity, hemostasis, angiogenesis and embryonic development. Integrin activation is regulated by large-scale conformational transitions from closed, low affinity states to open, high affinity states. While it has been suggested that substrate stiffness shifts the conformational equilibrium of integrin and governs its unbinding, here we address the role of integrin conformational activation in cellular mechanosensing. Comparison of WT vs activating mutants of integrin $\alpha_V\beta3$ show that activating mutants shift cell spreading, FAK activation, traction stress and force on talin toward high stiffness values at lower stiffness. Although all activated integrin mutants showed equivalent binding affinity for soluble ligands, the β3 S243E mutant showed the strongest shift in mechanical responses. To understand this behavior, we used coarse-grained computational models derived from molecular level information. The models predicted that wild type integrin $\alpha_V\beta3$ displaces under force, and that activating mutations shift the required force toward lower values, with S243E showing the strongest effect. Cellular stiffness sensing thus correlates with computed effects of force on integrin conformation. Together, these data identify a role for force-induced integrin conformational deformation in cellular mechanosensing.

Statement of Significance

Cells sense extracellular matrix stiffness through integrins to regulate many functions. Despite extensive study, major questions about molecular mechanisms remain unanswered. Here, we report evidence that direct effects of force on integrin conformation determine cellular stiffness sensing. These results are conceptually important because they identify integrins as true mechanosensors that determine signaling outputs.

Introduction

Integrin-based adhesions are the primary structures through which cells sense and respond to the physicochemical properties of the extracellular matrix, including variations in stiffness, composition, topology and spatial distribution (1). The ability of integrin-based adhesions to respond to matrix stiffness is critical for many cellular processes, including cell division (2), migration (3, 4), embryogenesis (5) and wound healing (6), among others. Variations in the stiffness of the extracellular matrix affect the assembly, binding properties, clustering and stability of integrins and integrin-based adhesions, and govern cell spreading and traction force (1, 7). Dysregulation of mechanosensing from integrin-based adhesions is associated with a wide variety of disorders, including cardiovascular disease (8, 9), musculoskeletal dysfunction (10), fibrosis (11), and cancer (3).

Integrins are heterodimeric transmembrane receptors that bidirectionally transmit mechanical and biochemical signals. They specifically bind components of the extracellular matrix, with each integrin dimer exhibiting a specific repertoire of ligands. Integrins exist in a range of affinity states whose interconversion from inactive to active involves long range transitions from bent to extended conformations (12). Conformational activation can be regulated through both intracellular activators (i.e. Rap1, talin, kindlin) and through extracellular matrix ligands (i.e. fibronectin, collagen), thus providing tight control of integrin engagement with the extracellular matrix.

Force applied to integrins facilitates a transition from bent to extended conformation, and contributes to the maintenance of the active conformation (13). Application of force to already activated, ligand-bound integrins induces additional

recruitment of intracellular adaptor molecules, adhesion reinforcement and growth (1, 7, 14, 15). Force on active, ligand-bound integrins also stabilizes the bound state, increases cellular traction force and spreading on surfaces, and activates downstream signaling pathways (16-18). These effects are generally attributed to transmission of force to talin, which then undergoes conformational transitions in which unfolding of helix bundle domains under tension triggers changes in binding partners, which both reinforces adhesions and regulates signaling (19). Other focal adhesion proteins such as p130Cas have also been proposed to function as direct mechanotransducers (20).

However, activating exogenous integrins with manganese ions increases cell spreading on soft surfaces that normally do not allow spreading (21). Integrin $\alpha_V\beta3$ is especially critical in cellular stiffness sensing (22). This integrin shows catch and then slip bond behavior as a function of force, where ligand-bond lifetimes for integrin increase with moderate force and then decrease at higher forces (23, 24). The idea that force either drives the conversion from inactive to active conformations or stabilizes the high affinity state, or both, suggests that integrin activation itself might play a role in mechanotransduction.

We therefore investigated the role of integrin conformation in stiffness sensing. Analysis of a collection of equivalently activated $\alpha_V\beta3$ mutants on elastic substrates of varying stiffness showed that these mutants shift cell spreading, activation of mechanosensitive signaling pathways (YAP, pFAK), traction forces and force on the central adhesion adaptor protein talin toward lower stiffness but to varying degrees. We then developed computational simulations based on coarse-grained modeling that utilize data from μs-long all-atom molecular dynamics simulations. The calculations

predict that the different mutants respond differently to force. Importantly, force-dependent transition to more extended conformations correlates closely with cellular stiffness sensing. These results identify a key role for force-induced integrin conformational deformation in cellular stiffness sensing.

Methods

Cell culture, transfection

Mouse lung endothelial cells (MLECs) isolated from β3 integrin null mice were generously provided by Mark Ginsberg and Brian Petrich (University of California at San Diego, CA) (25). β3 integrin single point mutants were generously provided by Timothy Springer (Harvard University, Boston MA) (26). These sequences were subcloned into pBOB vector and virus prepared in HEK 293Tx cells by co-transfecting with pCMV-VSV-G and psPAX2 using Lipofectamine 2000 (Invitrogen). The temperature sensitive mutant of the SV40 virus large T antigen was employed for conditional immortalization of these cells. Immortalized β3-/- MLECs were infected with wild-type (WT) or mutant β3 integrin viruses and subsequently sorted to obtain homogenous populations with equal expression levels (24). For expansion, MLECs were cultured in 1:1 Hams F-12 and high glucose DMEM with 20% FBS, 1% Penicillin-Streptomycin, 2.5mM glutamine and endothelial cell growth supplement (ECGS, 50mg/L) at the permissive temperature of 30°C. For experiments, cells were switched to 37°C to inactivate large T one day prior.

Polyacrylamide Substrate Preparation

Small polyacrylamide gels for imaging experiments were prepared as described (27). Briefly, 20mm coverslip bottom dishes (Mattek) were silanized with a 2% solution of 3-aminopropyltrimethoxysilane in isopropanol for 10 minutes at room temperature. After washing with ddH_2O and drying, coverslips were incubated with 1% glutaraldehyde solution in ddH_2O for 30 minutes and then washed 3 times. Polyacrylamide gels were cast onto the silanized surface by preparing acrylamide/bis-acrylamide solutions (Biorad) of various ratios (Supplemental Table 1) and polymerizing with ammonium persulfate (American bio) and TEMED (Sigma). Gels were cast between the silanized surface and a 12mm uncoated glass coverslips with a volume of 8ul. After casting, gels were treated with fresh sulfo-SANPAH (Sigma) in ddH_2O (2mg/ml) and exposed to UV light for 3 minutes (8W, 254 nm wavelength at a distance of 2-3 inches). After UV, gels were washed with ddH_2O and then covered with fibrinogen (200ug/ml in PBS at pH 7.4) overnight at 4ºC. Prior to seeding, gels were washed 3 times with PBS and pre-incubated with medium for 1 hour. Cell spreading experiments were performed in serum free conditions to prevent fibronectin deposition (High Glucose DMEM (Gibco) with 0.5% w/v bovine serum albumin (sigma), 1x Insulin-Transferrin-Selenium (ITS premix, Gibco)).

Larger polyacrylamide gels for western blot experiments were prepared using a modified version of the protocol from Elosegui A., et al (28). Briefly, 35-mm glass bottom dishes were activated with glacial acetic acid, 3-(trimethoxysilyl) propyl methacrylate, and 96% ethanol solution (1:1:14 ratio, respectively) for 10 minutes in room temperature. For fibrinogen conjugated gels, acrylamide was partially replaced with acrylic acid N-hydroxysuccinimide ester according to Supplemental Table 2, as

derived from (28). Cast gels were coated with fibrinogen (200ug/ml in PBS pH7.4) overnight at 4ºC. Cells were plated in serum free medium (High Glucose DMEM (Gibco) with 0.5% w/v bovine serum albumin (Sigma), 1x Insulin-Transferrin-Selenium (ITS premix, Gibco) to prevent FN deposition.

Cell Immunostaining and Quantification

Cells seeded on fibrinogen-coated glass or polyacrylamide were fixed with 4% paraformaldehyde (Electron Microscopy Sciences) in PBS. Cells were washed and permeabilized with 0.05% Triton X-100 in PBS supplemented with 320 mM sucrose and 6 mM $MgCl_2$, then washed 3 times with PBS and blocked for 30 minutes with 1% BSA in PBS. Cells were incubated overnight at 4°C with anti-YAP antibody (1:200, catalog number sc-101199, Santa Cruz Biotechnology) diluted in 1% BSA in PBS. Cells were washed 3 times with PBS and incubated at room temperature for 1 hour with secondary antibody (Alexa-647 anti-mouse, 1:1000, Molecular Probes) and Alexa-565 conjugated phalloidin (1:1000, Molecular Probes). They were washed again 3 times with PBS and mounted with DAPI in Fluoromount-G (Southern Biotech). Cell areas were quantified using ImageJ by background subtracting, thresholding to generate cell masks, and using the analyze particles function. YAP nuclear to cytosolic ratios were quantified by masking nuclear areas (DAPI) and cell areas (phalloidin) of interest in imageJ and then dividing the background-subtracted average signal in the nucleus by the average signal in the cytoplasm using MATLAB (Mathworks).

qPCR

Relative expression of CTGF versus β-actin was determined by rtPCR with primers for mouse actin (fw: 5'-cgagcgtggctacagcttc-3'; rv: 5'-gccatctcctgctcgaagtc-3'), and mouse CTGF (fw: 5'-ctgcagactggagaagcaga-3'; rv: 5'-gatgcacttttgcccttctt-3'). Cells were cultured on soft (3kPa) or stiff (30kPa) fibrinogen coated silicone gels for 24 hours in serum free media with fibronectin blocking antibody (16G3, 25ug/ml) with fresh antibody added at 0 and 12 hours to prevent cell deposited fibronectin from interfering. mRNA was isolated at 24 hours by directly lysing cells on the gel surface using the mRNeasy kit (Qiagen) and cDNA was synthesized using iScript cDNA synthesis kit (Biorad). PCR was run for 40 cycles on a Biorad CFX96 rtPCR machine using SsoAdvanced universal SYBR green supermix (Biorad).

Western Blot

MLECs seeded on PA gels were lysed directly in SDS sample buffer (100mM Tris-Cl pH6.8, 4% SDS, 0.2% Bromophenol Blue, 20% glycerol) with protease and phosphatase inhibitors (Halt protease inhibitor cocktail 100x, Thermo) and 2.5% beta-mercaptoethanol. Lysates were sonicated for 30 seconds and boiled at 95°C for 5 minutes. Samples were loaded onto 8% or 10% SDS-PAGE gels and run for 90 minutes at 120V in Tris-glycine buffer with SDS. Transfer was performed using Tris-Glycine 20% Methanol buffer onto nitrocellulose membranes (Biorad) with a Transblot Turbo (Biorad). Membranes were blocked with 5% BSA in Tris-buffered saline with 0.1% Tween 20 in 150mM NaCl, 50mM Tris-HCl, pH 7.6 (TBS-T) for 1 hour. Membranes were incubated overnight at 4°C with primary antibodies directed at total FAK (cell signaling 1:1000) or phosphorylated FAK (Y397, Cell Signaling, 1:1000) in

TBS-T. Membranes were washed 3 times for 5 minutes with TBS-T and incubated for 1 hour at room temp with peroxidase-conjugated anti-mouse or anti-rabbit secondary antibodies (1:4000 in TBS-T, vector labs). Membranes were washed 3 times for 5 minutes and bands were detected using Supersignal West Pico PLUS or Fempto detection reagents (Thermo) and imaged on a G:BOX gel imager (SYNGENE).

Traction Force Microscopy

Silicone TFM substrates were fabricated as described (29). Briefly, cover-glass bottom 96 well plates were spin-coated with a ~40µm thick layer of a silicone gel pre-polymer polydimethylsiloxane (CY 52-276 by Dow Inc., mixed at various A:B ratios, 1.4kPa = 0.8:1; 3.1kPa = 0.9:1; 11kPa = 1.2:1; 1.6:1 30kPa). Gel pre-polymer is cured by baking at 70°C overnight then treated with 3-aminopropyl trimethoxysilane for 5 min and incubated for 10 min at room temperature under a suspension of 40nm Alexa Fluor 647 beads (molecular probes) in a 100µg/ml solution of 1-Ethyl-3-(3-dimethylaminopropyl) carbodiimide (EDC, Sigma) in water to covalently link beads to the gel surface. Gel modulus for each batch was measured using a microfluidic device (29) and is reported as Young's elastic modulus (E).

TFM gels were coated with fibrinogen (10µg/ml) in PBS overnight at 4°C. Prior to seeding, gels were washed 3 times with PBS. Traction force experiments were performed in serum free conditions to limit fibronectin deposition (Phenol-Free High Glucose DMEM (gibco) with 0.5% w/v bovine serum albumin (Sigma), 1x Insulin-Transferrin-Selenium (ITS premix, gibco), and 1uM lysophosphatidic acid (Sigma). The day of the experiment, cells were trypsinized and seeded on TFM substrates at low

density (~3000 cells per cm^2) for 2 hours. Cells and florescent beads were imaged on a spinning disk confocal microscope (UltraVIEW VoX, Perkins Elmer) attached to a Nikon A-1 microscope equipped with a temperature and CO_2 controlled incubation chamber and 60x 1.4NA lens. Fluorescent images of Alexa Fluor 647 beads and DIC images of cells were acquired before and after cell lysis with 0.05% SDS. Images were drift corrected and bead displacements were quantified using a previously developed open source traction force microscopy software in MATLAB 2015a (26). Force fields and traction stresses were calculated using FTTC force reconstruction with regularization parameter set at (1kPa = 0.01, 3.1kPa = 0.001, 11kPa = 0.0001, 31kPa = 0.00005). Regularization parameter was chosen to give smooth traction maps and a single parameter was used for all groups at a given stiffness. Average stress per cell was calculated as the total force for a cell divided by its spread area.

FRET Imaging and Quantification

Quantification of FRET data was performed using the custom software in MATLAB we developed previously (30). All three FRET images (eGFP, tagRFP, FRET) were corrected for illumination gradient, pixel shift and background subtraction, followed by three-point smoothening. Bleed through and cross excitation co-efficients were calculated by imaging cells transfected with eGFP-talin or tagRFP-talin. The slope of the pixel-wise donor or acceptor channel intensity versus FRET channel intensity gives bleed through (x) or cross-excitation (y) fraction, respectively. Heat maps of FRET and pixel-wise FRET index were calculated using the following equation:

$$FRET\ Index = \frac{FRET - x(GFP) - y(RFP)}{RFP}$$

where FRET, GFP, and RFP are the shade, shift and background corrected pixel intensities for each of the respective channels. Average FRET Index was calculated for masked focal adhesions in each cell. Focal adhesion sizes for Talin tension sensor images were quantified using the focal adhesion analysis server (FAAS) (31) with default settings for static properties only and for adhesions greater than 0.2μm^2.

Computational Models of Active $\alpha_V\beta_3$ Integrin under Force

We used a CG computational model in order to study the effect of force on wild type $\alpha_V\beta3$ integrin and the L138I, K417E, and S243E mutants. Starting from µs-long equilibrium all-atom molecular dynamics simulations, we decreased the representation of each integrin from 1780 Cα atoms to 300 CG beads (average resolution 8 ± 4 Cα atoms per CG bead), using the Essential Dynamics Coarse Graining approach (32). Each CG bead of bent $\alpha_V\beta_3$ was placed at the center of geometry of the corresponding Cα atoms of open $\alpha_{IIB}\beta_3$ integrin (33). Then, CG beads were connected using effective harmonic and Morse interaction potentials by applying our recent hENM-based approach (for details, see (34) and SI). Lastly, we ran Langevin Dynamics using the molecular dynamics software LAMMPS (35), with the temperature set at 310 K, with a constant number of particles, volume, and temperature (NVT) ensemble. In order to mimic the effect of the cell membrane, transmembrane helices were spatially restrained; to mimic the effect of substrate rigidity, a pulling force was applied on the ligand binding site. For outputs, we analyzed structural parameters representative of conformational stability of integrin, including overall integrin length and separation between the two integrin legs.

Backmapping of Coarse-grained to All-atom models

The initial atomic model for WT integrin was constructed from structures obtained via x-ray crystallography and solution NMR (3IJE.pdb (36) and 2KNC.pdb (37)). Missing amino acid backbones were built using MODELLER (38), and missing side chains were optimized using SCWRL4 (39). In the all-atom model of integrin, center-of-mass (COM) positions of atoms belonging to each CG particle were computed of the unloaded CG system. The COM positions were grouped on the basis of distinct secondary structural elements of the protein. For each secondary structural element, rotation and translation matrices were computed by minimizing the RMSD in a rigid-body fit of the COM positions to the CG conformation of WT integrin derived from the CG MD simulations without force. These transformation matrices were then applied to the corresponding all-atom model for each secondary structural element to generate an initial backmapped model (Sup. Fig. 5A-B). The backmapped all-atom structures were subsequently refined using steepest descent and adopted basis Newton Raphson energy minimization algorithms in the CHARMM36 force field (40, 41). The same backmapping procedure was repeated for the S243E integrin mutant and the corresponding CG conformation derived from the CG MD simulations. The backmapped all-atom structures were inserted into a lipid bilayer with 80% DOPC and 20% DOPS lipids (960 lipids in each leaflet, total 1920 lipids in membrane) using CHARMM-GUI membrane builder (33). Similar to the initial AA MD simulations, the lipid-membrane/integrin systems were hydrated with TIP3P water molecules and 150 mM NaCl, for a total of about 1.9 million atoms for wild type integrin and 2.2 million atoms for S243 mutant. The sizes of these

systems were significantly larger than the initial AA systems, owing to the more extended and open configurations of stretched integrin, which occupy a larger volume in the computational domain. Energy minimization was run for 5000 steps of steepest descent algorithm, then equilibration was performed to relax the system. We used a six-step protocol where decreasing restraints were applied to the protein, lipids and water molecules: NVT dynamics (constant volume and temperature) was used for the first two steps, followed by NPAT dynamics (constant pressure, area and temperature) for the rest, at 310 K. At the end of equilibration, we analyzed structural properties of AA wild type and S243 mutant integrins. Consistent with the structural properties of the stretched coarse-grained structures, comparison of stretched wild type integrin to the S243E mutant showed a more bent headpiece (122 deg +/- 7.8 deg for WT genu angle vs166 deg +/- 18.3 for S243E) and closer chains (genu separation 7.6 nm +/- 0.4 nm for WT vs 4.7 nm +/- 1.1nm for S243E), see Fig 5C-D. Constant-force steered MD was done on the backmapped all-atom systems and revealed that the S243E mutant extended more than WT under force (Fig. 5E-F). These results indicate that the structural properties of the CG systems are maintained at the molecular levels in stretched integrins and provide further evidence that force stabilizes extended integrin conformations.

Steered Molecular Dynamics of Backmapped All-atom integrin models

In order to evaluate the effect of an external force on the extension of all-atom integrin, we performed Steered Molecular Dynamics simulations (SMD) on the backmapped and energy minimized AA wild type and S243 mutants. A constant vertical force of 1 or 10

pN was applied to the center of mass of the ligand binding site, while the β chain transmembrane helix was held fixed within the lipid bilayer. The simulations were performed using Gromacs 5.0.4 (42), for 500 ps in the NPT ensemble using Berendsen barostat (43), keeping the temperature at 310 K and pressure at 1 atm with semi-isotropic pressure coupling with a compressibility of $4.5 \times 10^{-5} bar^{-1}$. Long-range electrostatic interactions were incorporated through the Particle Mesh Ewald (PME) method with a cut-off of 1 nm (44). Analysis of extension at 1 pN or 10 pN constant force was performed.

Statistics

All of the statistical analysis was performed using Prism version 7.01 (Graphpad). Details regarding the specific statistical tests used, the sample size, p values, and number of independent experiments are provided in the figure legends. All experimental data are included in the supplemental data spreadsheet. Modeling results are available at https://github.com/tamarabidone/integrins_AA_CG.

Results

Activating mutants drive cell spreading on soft substrates

To assess the effects of activating mutations on stiffness sensing, we expressed wild type β3 integrin or activated mutants (L138I, S243E, K417E) (45) in immortalized β3 integrin knockout mouse lung endothelial cells (MLECs). Previous studies used binding to the monomeric high affinity soluble ligand WOW-1 as the optimal assay for

integrin affinity without interference from clustering and in the absence of force (46). These results showed that the mutations resulted in increased affinity that was indistinguishable between the mutants (34). To assess spreading and YAP nuclear localization as typical stiffness-dependent functions, polyacrylamide gels of varying stiffnesses were coated with the β3 ligand fibrinogen. $\beta3^{-/-}$ cells show minimal adhesion to these surfaces, demonstrating specificity. Cells expressing equivalent levels of wild type (WT) or mutant β3 were plated and assayed at 3 hours to minimize fibrinogen proteolysis or other modifications of the substrates. WT β3 cells adhered well and showed the expected stiffness-dependent increase in spread area and YAP nuclear localization (Fig. 1A,B and Sup. Fig. 1). Activating mutations shifted the ability of cells to spread and induce YAP nuclear localization toward lower stiffnesses (Fig. 1A-C). Interestingly, L138I had only a weak effect whereas S243E and K417E strongly shifted the behavior toward softer substrates without increasing maximal cell spreading or YAP nuclear localization on stiff substrate. These results were confirmed by quantification of the YAP target gene CTGF (Sup. Fig. 2A), which showed increased expression for all mutants on soft (3kPa) gels. Integrin activation thus promotes spreading on soft substrates, confirming the results with Mn2+ activation of integrin (21). Additionally, our results show that the mechanosensitive YAP pathway is similarly regulated.

Activating mutants and tyrosine phosphorylation

We next assessed phosphorylation of focal adhesion kinase (FAK) on tyrosine 397, a well-established mechanosensitive event, in cells plated on gels of different stiffness. As expected (47, 48), cells expressing WT β3 showed increasing pFAK (Fig.

2A-B) with increasing stiffness. All of the activating β3 mutations showed non-significant trends toward higher phosphorylation of FAK (Fig. 2B) in suspension, which we take as the baseline levels. Importantly, the S243E mutant showed a large and significant increase in pFAK/tFAK at low stiffness (0.5kPa) (Fig. 2B). We also analyzed these curves by calculating the effective stiffness required for 50% maximal FAK activation, YAP nuclear translocation, and cell spreading (ES50 for these variables). This metric revealed downward shifts in the threshold for stiffness-dependent activation for all mutants, with S243E having the most consistent and largest effect for all three outputs (Sup. Fig. 2B). While this approach provides a simple, convenient way to quantify the shift in stiffness sensitivity, it may underestimate the actual difference due the fact that the WT group did not reach saturation at the highest stiffness values.

Activating mutants and traction force

To assay the mechanical forces at the cellular length scale, we measured traction stresses as a function of substrate stiffness (1.4, 3.1, 11, 31 kPa). Cells plated on fibrinogen-coated silicone gels containing fluorescent beads were imaged before and after cell lysis. Cell-induced bead deformations were analyzed to generate heatmaps of traction stress (Fig. 3A, Sup. Fig. 3A-D) which were cropped for the area occupied by the cell to calculate average traction stress per cell (Fig. 3B). Measurements were performed 2 hours after seeding, when traction forces stabilize but are specific to β3 integrin (Sup. Fig. 2C). Cells expressing WT β3 showed increasing traction stress with increasing stiffness, as expected (28). The L138I and K417E mutants showed only slightly elevated stresses at the intermediate stiffnesses (Fig. 3B). By contrast, the

S243E mutant showed maximal traction stress at low stiffness with no further increase (Fig. 3B). Traction forces are well known to increase as a function of cell spreading (49). Reporting these values as stress, which is force per unit area, partly accounts for this effect. That traction stresses for the L138E and K417E mutants are not significantly different from WT β3 indicates that their increased cell spreading on soft substrates largely accounts for the resultant increase in traction force. By contrast, S243E significantly increasing traction stress, especially at low stiffness, meaning that the increase in force is greater than what would be expected for the increased spreading.

With accumulating evidence that the S243E mutation uniquely influences forces at the cellular scale, these effects might conceivably be due to recruitment of a greater number of activated integrins to the adhesions. To exclude such effects, we used a previously developed FRET-based tension sensor which uses a FRET pair (eGFP and mRFP) separated by an elastic peptide linker that reports force/molecule (50). To assay force on talin, the central focal adhesion protein that links integrins to F-actin, we used the previously characterized tension sensor in which the module was inserted between the head domain that binds the integrin β tail and the rod domain that binds F-actin (30). Force on talin results in separation of the FRET pair and decreased FRET efficiency. These results were compared to the control FRET sensor (CTS) in which the module is fused to the C-terminus; this construct localizes similarly but is not exposed to force. A previous study (30) validated the force-sensitivity of the probe and showed that force on talin is diminished on soft substrates. We simultaneously measured force on talin (FRET index) and average traction stress (Fig. 3C) on soft (1.4kPa) silicone gels in the same cells. The S243E mutant showed the highest traction stress (Fig. 3D) and the

lowest FRET index (Fig. 3E, Sup. Fig. 2G), indicating the highest force on talin. On glass, which is very stiff, there was a trend toward higher talin tension in S243E cells but it did not reach significance (Sup. Fig. 2D and 2E). Measurement of focal adhesion size showed that the S243E displayed larger talin adhesions on soft gels but similar focal adhesion sizes on glass (Sup. Fig. 2D and 2F). Together, multiple assays indicate that the S243E activating mutation induces high stiffness responses on soft gels, thus, appears to sensitize cells to low forces.

Computational analysis of Integrin mechanical properties

To investigate how integrin activating mutations alter stiffness sensing at the length scale of individual integrins, we built computational simulations using a coarse-grained (CG) modeling approach built "bottom-up" from all-atom molecular dynamics data converted into hetero-elastic network models (hENM) (Fig. 4A-B) (51). Integrins were represented by CG "beads" representing groupings of amino acids interconnected by effective harmonic and anharmonic potentials (Fig. 4B), according to our recently developed method (34). Force, *F*, was applied to the ligand binding site in the β headpiece (Fig. 4B) and the subsequent changes for each mutant were evaluated (Fig. 4C). We first used $F = 0$ pN as the starting point and $F = 1$ pN to mimic soft substrates/low force. Although catch bond behavior has not been analyzed for integrin avb3, studies of LFA1 (aLb2) detected catch bond in the low pN range (52), similar to the values used here. Simulations were then run for 1 μs. The root means square displacement (RMSD) of the integrin, computed as the averaged displacement of all the beads, was then evaluated for each mutant. All of the activating mutants exhibited

increased displacement (movement away from the starting positions during the simulation) under this low force compared to WT, with the difference being somewhat higher for S243E relative to the other mutants (Fig. 4D). S243E also presented significantly lower elastic constants and equilibrium separations between CG beads (Sup. Fig. 4A-C), resulting in higher conformational flexibility (Sup. Fig. 4D) and headpiece fluctuations (Sup. Fig. 4E). Under 0 or low (1 pN) force, the mutant integrins were more extended than wild type, with the mutant S243E showing the largest effect (Fig. 4E). At higher forces (3 and 5pN), all constructs showed significant increases in RMSD (Fig. 4D).

Integrin activation at the ligand binding site is communicated to the cytoplasmic domains via a long-range conformation change that separates the legs of the α and β subunits, leading to intracellular signaling (53). Separation of the legs is thus linked to activation. This distance, measured at the genu region, was highest for S243E under 0 pN force and did not increase further (Fig. 4F and Sup. Fig. 4D), consistent with the increased signaling under conditions of low force. S243E also showed increased force-extension relations (Sup. Fig. 4F-G). To assess the validity of the tension-dependent CG configurations, we backmapped wild type and S243E into atomistic models, which were energy minimized and equilibrated with all-atom MD in lipid membranes, then subjected to constant-force steered molecular dynamics simulations. These structures exhibited no steric clashes between lateral chains (Fig. 5A-D) and S243E integrin extended more than wild type under force (Fig. 5E-F). Together, these results show that the activating integrin mutant S243E is uniquely responsive to soft substrates due to its enhanced protein extension and flexibility under low forces.

Discussion

The ability of cells to sense the mechanical properties of their extracellular matrix through integrins is critical for cell differentiation, migration, tissue mechanical homeostasis and other functions (1-6). Due to their critical role in creating the physical link between cells and extracellular matrix, integrins are a key component of matrix mechanosensing (1, 15). But whether integrins are true mechanotransducers, that is, proteins whose conformational transitions under force are critical to signaling, is unknown. Published work has focused on talin (28), vinculin (16), FAK (47) , YAP (54), or integrin type (17) as the main determinant of stiffness sensing and mechanotransduction. However, it is known that integrin-ligand bonds stabilize under moderate forces, exhibiting so-called catch bond behavior (23). A previous study using manganese to activate integrins suggested a role for integrin activation in stiffness sensing (21), We therefore investigated the role of integrin conformation in mechanosensing in greater detail.

Here, we report a correlation between integrin conformational flexibility at the single molecule level and cellular stiffness sensing. For the endothelial cells used in this study, the transition in spreading, traction force and signaling is centered around 3-5 kPa, with those functions reaching a plateau above ~10 kPa, similar to published data for other adherent, well spread cell types (28, 47, 48). We also show that downstream mechanosensory pathways are impacted by this activation on soft gels, directly implicating integrin activation as a “mechanosensor”. However, examination of several β3 mutants revealed distinct effects on cellular mechanosensing that cannot be explained by differences in simple binding affinity, i.e., in the absence of force. Instead,

the S243E mutant had strong effects in multiple assays despite an equivalent increase in binding of soluble ligand (34).

Understanding these results requires analysis of effects of force on integrin conformation. However, this goal is not experimentally accessible. We therefore used our recently developed CG simulation approach to address how integrin conformation changes under tension. The benefit of the CG model is its ability to sample large conformational changes by explicitly incorporating breakage of effective bonds between CG beads from atomistic fluctuations. By taking interaction parameters directly from all-atom molecular dynamics simulations, our hENM-based CG model implicitly incorporates the effects of single point mutations on residue motions into the strength and functional forms of the interactions between beads in the CG systems. Consequently, when force is applied between the ligand binding site and the cytoplasmic domain, all CG integrins examined here extend and rearrange their beads on the headpiece chains relative to lower legs. In particular, WT αVβ3 extended, consistent with increased activation of integrins under tension. By contrast, all of the activating mutations increased length in the absence of tension (“resting" length) with further increases upon application of tension, with the S243E mutant showing the largest effect. It is noteworthy that both experimental and simulation data show that the mutations induce a leftward shift in the force-dependence, which is greatest for S243E.

Together, these results provide evidence that integrin conformational activation is not only force dependent but imparts mechanosensitivity that determines multiple signaling outputs, including cell spreading, YAP and FAK activation and exertion of traction force. These effects fit well with the widely accepted model in which early

integrin outside-in signaling promotes adhesion reinforcement to amplify subsequent events such as activation of tyrosine kinases, RhoA and cell contractility, which increase additional downstream signals such as Yap/Taz (55, 56). These findings thus indicate that integrin αVβ3 is a true mechanosensor. Many studies have implicated integrins in mechanosensory processes and previous modeling work has identified that force accelerates hinge-angle opening from inactive to active states (57). However, the importance of force induced deformation of the active and ligand bound integrin in mechanosensing, meaning regulation of signaling pathways, has not to our knowledge been previously demonstrated.

Although not accessible by the methods used here, it seems likely that integrin catch bond behavior plays a significant role in these processes. Thus, the S243E mutant may convert to high affinity or long lived states at lower force thresholds. In any case, bond lifetime information must be relayed to the cell interior to regulate signaling pathways. Integrins are well suited for this function as conformational effects are transmitted over long distances to the cytoplasmic domain. Leg separation distance may also be an important regulator of intracellular binding and our modeling results indicate that the S243E mutant has the largest leg separation distance at 0 and 1 pN applied force. The interaction with talin is an obvious candidate but contributions from other proteins that interact with integrin cytoplasmic domains are also likely. The ILK-PINCH-parvin complex and kindlins are also implicated in mechanosensing and could thus mediate effects. Understanding how alterations in integrin conformation affect both extracellular and intracellular binding interactions is the major direction for future work.

Author contributions: M.A.S., G.A.V., T.P.D., and T.C.B designed the research; T.P.D., T.C.B., and S.A. performed the research; T.P.D., T.C.B, A.G., and G.A.V. contributed new regents/analytic tools; T.P.D. and T.C.B. analyzed the data; A.Y. and T.C.B. performed the backmapping. T.P.D., T.C.B and M.A.S. wrote the paper.

Acknowledgments

This work was supported through the Department of Defense Army Research Office through a Multidisciplinary Research Initiative Grant W911NF1410403 to MAS and GAV, and an NIH fellowship F32GM119286 to TPD. Computer time was provided by the National Science Foundation XSEDE resources at the Pittsburgh Supercomputing Center and the Center for High Performance Computing at the University of Utah. We thank Anirban Polley and Timothy Loose for their help with the molecular dynamics simulations.

Figure Legends

Figure 1: Integrin activating mutants increase spreading and YAP nuclear localization at low stiffness.

(A) Cell spread area 3 hours after seeding on fibrinogen-coated polyacrylamide of the indicated Young's Modulus. Area was quantified from area of phalloidin-stained β3 KO MLECs reconstituted with the indicated β3 Integrin. Vales are means ± SEM, n= 25-123 Cells per group from two independent experiments, * $p<0.05$, ** $p<0.01$, *** $p<0.001$, # $p<0.05$ vs WT at same stiffness, two-way ANOVA with Tukey's post hoc (KO cells n=10-25 due to limited adhesion). **(B)** Quantification of the ratio of nuclear to cytoplasmic YAP signal at each stiffness. Values are means ± SEM, n=25-123 cells per group from two independent experiments, * $p<0.05$, *** $p<0.001$, two-way ANOVA with Tukey's post hoc. **(C)** Representative images of F-Actin (Phalloidin), YAP, and DAPI staining for MLECs on 0.6kPa gels (scale bar = 50µm)

Figure 2: FAK phosphorylation.

(A) Western blots for phosphorylated FAK (Y397) normalized to total FAK on fibrinogen-coated polyacrylamide gels of the indicated stiffness (S= suspension) for β3 KO MLECs reconstituted with WT or mutant β3 Integrin (L138I, S243E, K417E activating mutations). **(B)** Densitometry of phosphorylated FAK normalized for total FAK. Values are means ± SEM, n=4 independent experiments, # $p<0.05$, one-way non-parametric ANOVA with Dunn's multiple comparison.

Figure 3: Traction stresses and force on talin.

(A) Heat maps for traction stress for MLECs with WT or mutant β3 integrin on fibrinogen-coated silicone surfaces of the indicated stiffness. Surfaces were coated with fluorescent beads (Alexa-647) and bead displacements were tracked before and after cell lysis for calculation of stresses which were cropped for the area of the cell (outlined in yellow, scale bar = 10µm). **(B)** Quantification of average traction stress per cell for WT and mutant reconstituted cells. Values are means ± SEM, n=33-41 cells per group from 3 independent experiments, ** $p<0.01$, *** $p<0.001$, **** $p<0.0001$, two-way ANOVA with Dunnett's multiple comparison). **(C)** Heat maps of traction stress (left) and FRET index of talin tension sensor (middle) with images of GFP-talin focal adhesions (right) for experiments with simultaneous measurement of traction force and force on talin on soft fibrinogen coated silicone surfaces (1.4kPa) (scale bar = 10µm). **(D)** Quantification of average traction stress per cell. Values are means ± SEM, n=7-10 cells per group from two independent experiments, ## $p=0.0119$, one-way ANOVA with Dunnett's multiple comparison). **(E)** Quantification of average FRET index per cell. Values are means ± SEM, n=7-10 cells per group from two independent experiments, # $p=0.0286$, ## $p<0.001$, one-way ANOVA with Dunnett's multiple comparison, CTS indicates talin C-terminal control sensor expressed in WT cells).

Figure 4. Computational analysis of integrin conformation.

(A) Ribbon representation of bent integrin, with point mutations in the hybrid or βA domain highlighted. **(B)** hENM extended integrin, with CG beads of α and β chain in red and blue, respectively. **(C)** Snapshots from timestep 10 of the simulations under 1 pN

force, where the mutants (cyan, magenta and blue) are overlaid to WT (in red). **(D)** Average root mean square (RMS) displacements for WT and mutant integrins at F = 0-5 pN with respect to WT integrin at F = 0 pN. **(E)** Average length of WT and mutant integrins at F = 0 and 1pN. **(F)** Leg distance at F = 0-5 pN, normalized by WT integrin at F = 0 pN, computed as average of the center of mass distance between the two transmembrane helices. All mean values are computed between 30-300 timesteps of simulations. Values are means ± SEM, $p<0.0001$.

Figure 5. All-atom backmapped structures of WT and S243E under force.

All-atom backmapped configurations for **(A)** wild type and **(B)** S243E integrins, after energy minimization. CG beads (in orange) and secondary structure elements (in blue and red, to distinguish between the two chains) are superimposed. AA backmapped configurations for integrins in the absence of force, embedded in multicomponent lipid bilayer, after energy minimization and equilibration: **(C)** wild type and **(D)** S243E mutant are shown in ribbon representation; lipids are shown in VDW representation. Boxplots of extension under constant force for WT and mutant integrins (computed between 100-200 ps of constant-force steered molecular dynamics simulations), normalized by the average extension of integrin without force (computed between 1-20 ns of equilibrium simulations). These values are extracted from backmapped all-atom models of WT and mutant integrins at 1 pN **(E)** and 10 pN **(F)** force. (box plots indicate median, 25th and 75th percentile, min and max, *** $p<0.001$, unpaired t-test).

References

1. Kechagia, J. Z., J. Ivaska, and P. Roca-Cusachs. 2019. Integrins as biomechanical sensors of the microenvironment. Nat Rev Mol Cell Biol.
2. Chen, C. S., M. Mrksich, S. Huang, G. M. Whitesides, and D. E. Ingber. 1997. Geometric control of cell life and death. Science 276:1425-1428.
3. Wisdom, K. M., K. Adebowale, J. Chang, J. Y. Lee, S. Nam, R. Desai, N. S. Rossen, M. Rafat, R. B. West, L. Hodgson, and O. Chaudhuri. 2018. Matrix mechanical plasticity regulates cancer cell migration through confining microenvironments. Nat Commun 9:4144.
4. Kiosses, W. B., S. J. Shattil, N. Pampori, and M. A. Schwartz. 2001. Rac recruits high-affinity integrin alphavbeta3 to lamellipodia in endothelial cell migration. Nat Cell Biol 3:316-320.
5. Barriga, E. H., K. Franze, G. Charras, and R. Mayor. 2018. Tissue stiffening coordinates morphogenesis by triggering collective cell migration in vivo. Nature 554:523-527.
6. Kenny, F. N., and J. T. Connelly. 2015. Integrin-mediated adhesion and mechano-sensing in cutaneous wound healing. Cell Tissue Res 360:571-582.
7. Case, L. B., and C. M. Waterman. 2015. Integration of actin dynamics and cell adhesion by a three-dimensional, mechanosensitive molecular clutch. Nat Cell Biol 17:955-963.
8. Finney, A. C., K. Y. Stokes, C. B. Pattillo, and A. W. Orr. 2017. Integrin signaling in atherosclerosis. Cell Mol Life Sci 74:2263-2282.
9. Hahn, C., and M. A. Schwartz. 2009. Mechanotransduction in vascular physiology and atherogenesis. Nat Rev Mol Cell Biol 10:53-62.
10. Mayer, U., G. Saher, R. Fassler, A. Bornemann, F. Echtermeyer, H. von der Mark, N. Miosge, E. Poschl, and K. von der Mark. 1997. Absence of integrin alpha 7 causes a novel form of muscular dystrophy. Nat Genet 17:318-323.
11. Wipff, P. J., D. B. Rifkin, J. J. Meister, and B. Hinz. 2007. Myofibroblast contraction activates latent TGF-beta1 from the extracellular matrix. J Cell Biol 179:1311-1323.
12. Shattil, S. J., C. Kim, and M. H. Ginsberg. 2010. The final steps of integrin activation: the end game. Nat Rev Mol Cell Biol 11:288-300.
13. Jin, M., I. Andricioaei, and T. A. Springer. 2004. Conversion between three conformational states of integrin I domains with a C-terminal pull spring studied with molecular dynamics. Structure 12:2137-2147.
14. Wolfenson, H., I. Lavelin, and B. Geiger. 2013. Dynamic regulation of the structure and functions of integrin adhesions. Dev Cell 24:447-458.
15. Jansen, K. A., P. Atherton, and C. Ballestrem. 2017. Mechanotransduction at the cell-matrix interface. Semin Cell Dev Biol 71:75-83.
16. Carisey, A., R. Tsang, A. M. Greiner, N. Nijenhuis, N. Heath, A. Nazgiewicz, R. Kemkemer, B. Derby, J. Spatz, and C. Ballestrem. 2013. Vinculin regulates the recruitment and release of core focal adhesion proteins in a force-dependent manner. Current biology : CB 23:271-281.
17. Elosegui-Artola, A., E. Bazellieres, M. D. Allen, I. Andreu, R. Oria, R. Sunyer, J. J. Gomm, J. F. Marshall, J. L. Jones, X. Trepat, and P. Roca-Cusachs. 2014. Rigidity sensing and adaptation through regulation of integrin types. Nat Mater 13:631-637.
18. Astrof, N. S., A. Salas, M. Shimaoka, J. Chen, and T. A. Springer. 2006. Importance of force linkage in mechanochemistry of adhesion receptors. Biochemistry 45:15020-15028.
19. Goult, B. T., J. Yan, and M. A. Schwartz. 2018. Talin as a mechanosensitive signaling hub. J Cell Biol 217:3776-3784.
20. Moore, S. W., P. Roca-Cusachs, and M. P. Sheetz. 2010. Stretchy proteins on stretchy substrates: the important elements of integrin-mediated rigidity sensing. Dev Cell 19:194-206.

21. Oakes, P. W., T. C. Bidone, Y. Beckham, A. V. Skeeters, G. R. Ramirez-San Juan, S. P. Winter, G. A. Voth, and M. L. Gardel. 2018. Lamellipodium is a myosin-independent mechanosensor. Proc Natl Acad Sci U S A 115:2646-2651.
22. Roca-Cusachs, P., N. C. Gauthier, A. Del Rio, and M. P. Sheetz. 2009. Clustering of alpha(5)beta(1) integrins determines adhesion strength whereas alpha(v)beta(3) and talin enable mechanotransduction. Proc Natl Acad Sci U S A 106:16245-16250.
23. Kong, F., A. J. Garcia, A. P. Mould, M. J. Humphries, and C. Zhu. 2009. Demonstration of catch bonds between an integrin and its ligand. J Cell Biol 185:1275-1284.
24. Chen, Y., H. Lee, H. Tong, M. Schwartz, and C. Zhu. 2017. Force regulated conformational change of integrin alphaVbeta3. Matrix Biol 60-61:70-85.
25. Liao, Z., H. Kato, M. Pandey, J. M. Cantor, A. J. Ablooglu, M. H. Ginsberg, and S. J. Shattil. 2015. Interaction of kindlin-2 with integrin beta3 promotes outside-in signaling responses by the alphaVbeta3 vitronectin receptor. Blood 125:1995-2004.
26. Han, S. J., Y. Oak, A. Groisman, and G. Danuser. 2015. Traction microscopy to identify force modulation in subresolution adhesions. Nat Methods 12:653-656.
27. Aratyn-Schaus, Y., P. W. Oakes, J. Stricker, S. P. Winter, and M. L. Gardel. 2010. Preparation of complaint matrices for quantifying cellular contraction. J Vis Exp.
28. Elosegui-Artola, A., R. Oria, Y. Chen, A. Kosmalska, C. Perez-Gonzalez, N. Castro, C. Zhu, X. Trepat, and P. Roca-Cusachs. 2016. Mechanical regulation of a molecular clutch defines force transmission and transduction in response to matrix rigidity. Nat Cell Biol 18:540-548.
29. Gutierrez, E., and A. Groisman. 2011. Measurements of elastic moduli of silicone gel substrates with a microfluidic device. PLoS One 6:e25534.
30. Kumar, A., M. Ouyang, K. Van den Dries, E. J. McGhee, K. Tanaka, M. D. Anderson, A. Groisman, B. T. Goult, K. I. Anderson, and M. A. Schwartz. 2016. Talin tension sensor reveals novel features of focal adhesion force transmission and mechanosensitivity. J Cell Biol 213:371-383.
31. Berginski, M. E., and S. M. Gomez. 2013. The Focal Adhesion Analysis Server: a web tool for analyzing focal adhesion dynamics. F1000Res 2:68.
32. Zhang, Z., L. Lu, W. G. Noid, V. Krishna, J. Pfaendtner, and G. A. Voth. 2008. A systematic methodology for defining coarse-grained sites in large biomolecules. Biophys J 95:5073-5083.
33. Xu, X. P., E. Kim, M. Swift, J. W. Smith, N. Volkmann, and D. Hanein. 2016. Three-Dimensional Structures of Full-Length, Membrane-Embedded Human alpha(IIb)beta(3) Integrin Complexes. Biophys J 110:798-809.
34. Bidone, T. C., A. Polley, J. Jin, T. Driscoll, D. V. Iwamoto, D. A. Calderwood, M. A. Schwartz, and G. A. Voth. 2019. Coarse-Grained Simulation of Full-Length Integrin Activation. Biophys J 116:1000-1010.
35. Plimpton, S. 1995. Fast Parallel Algorithms for Short-Range Molecular-Dynamics. J Comput Phys 117:1-19.
36. Xiong, J. P., B. Mahalingham, J. L. Alonso, L. A. Borrelli, X. Rui, S. Anand, B. T. Hyman, T. Rysiok, D. Muller-Pompalla, S. L. Goodman, and M. A. Arnaout. 2009. Crystal structure of the complete integrin alphaVbeta3 ectodomain plus an alpha/beta transmembrane fragment. J Cell Biol 186:589-600.
37. Yang, J., Y. Q. Ma, R. C. Page, S. Misra, E. F. Plow, and J. Qin. 2009. Structure of an integrin alphaIIb beta3 transmembrane-cytoplasmic heterocomplex provides insight into integrin activation. Proc Natl Acad Sci U S A 106:17729-17734.
38. Webb, B., and A. Sali. 2016. Comparative Protein Structure Modeling Using MODELLER. Curr Protoc Bioinformatics 54:5 6 1-5 6 37.
39. Krivov, G. G., M. V. Shapovalov, and R. L. Dunbrack, Jr. 2009. Improved prediction of protein side-chain conformations with SCWRL4. Proteins 77:778-795.

40. MacKerell, A. D., D. Bashford, M. Bellott, R. L. Dunbrack, J. D. Evanseck, M. J. Field, S. Fischer, J. Gao, H. Guo, S. Ha, D. Joseph-McCarthy, L. Kuchnir, K. Kuczera, F. T. Lau, C. Mattos, S. Michnick, T. Ngo, D. T. Nguyen, B. Prodhom, W. E. Reiher, B. Roux, M. Schlenkrich, J. C. Smith, R. Stote, J. Straub, M. Watanabe, J. Wiorkiewicz-Kuczera, D. Yin, and M. Karplus. 1998. All-atom empirical potential for molecular modeling and dynamics studies of proteins. J Phys Chem B 102:3586-3616.
41. Best, R. B., X. Zhu, J. Shim, P. E. Lopes, J. Mittal, M. Feig, and A. D. Mackerell, Jr. 2012. Optimization of the additive CHARMM all-atom protein force field targeting improved sampling of the backbone phi, psi and side-chain chi(1) and chi(2) dihedral angles. J Chem Theory Comput 8:3257-3273.
42. Pall, S., M. J. Abraham, C. Kutzner, B. Hess, and E. Lindahl. 2015. Tackling Exascale Software Challenges in Molecular Dynamics Simulations with GROMACS. Lect Notes Comput Sc 8759:3-27.
43. Parrinello, M., and A. Rahman. 1981. Polymorphic Transitions in Single-Crystals - a New Molecular-Dynamics Method. J Appl Phys 52:7182-7190.
44. Darden, T., D. York, and L. Pedersen. 1993. Particle Mesh Ewald - an N.Log(N) Method for Ewald Sums in Large Systems. J Chem Phys 98:10089-10092.
45. Luo, B. H., J. Karanicolas, L. D. Harmacek, D. Baker, and T. A. Springer. 2009. Rationally designed integrin beta3 mutants stabilized in the high affinity conformation. J Biol Chem 284:3917-3924.
46. Pampori, N., T. Hato, D. G. Stupack, S. Aidoudi, D. A. Cheresh, G. R. Nemerow, and S. J. Shattil. 1999. Mechanisms and consequences of affinity modulation of integrin alpha(V)beta(3) detected with a novel patch-engineered monovalent ligand. J Biol Chem 274:21609-21616.
47. Bae, Y. H., K. L. Mui, B. Y. Hsu, S. L. Liu, A. Cretu, Z. Razinia, T. Xu, E. Pure, and R. K. Assoian. 2014. A FAK-Cas-Rac-lamellipodin signaling module transduces extracellular matrix stiffness into mechanosensitive cell cycling. Sci Signal 7:ra57.
48. Zaidel-Bar, R., R. Milo, Z. Kam, and B. Geiger. 2007. A paxillin tyrosine phosphorylation switch regulates the assembly and form of cell-matrix adhesions. J Cell Sci 120:137-148.
49. Fu, J., Y. K. Wang, M. T. Yang, R. A. Desai, X. Yu, Z. Liu, and C. S. Chen. 2010. Mechanical regulation of cell function with geometrically modulated elastomeric substrates. Nat Methods 7:733-736.
50. Grashoff, C., B. D. Hoffman, M. D. Brenner, R. Zhou, M. Parsons, M. T. Yang, M. A. McLean, S. G. Sligar, C. S. Chen, T. Ha, and M. A. Schwartz. 2010. Measuring mechanical tension across vinculin reveals regulation of focal adhesion dynamics. Nature 466:263-266.
51. Lyman, E., J. Pfaendtner, and G. A. Voth. 2008. Systematic multiscale parameterization of heterogeneous elastic network models of proteins. Biophys J 95:4183-4192.
52. Chen, W., J. Lou, and C. Zhu. 2010. Forcing switch from short- to intermediate- and long-lived states of the alphaA domain generates LFA-1/ICAM-1 catch bonds. J Biol Chem 285:35967-35978.
53. Hu, P., and B. H. Luo. 2013. Integrin bi-directional signaling across the plasma membrane. J Cell Physiol 228:306-312.
54. Dupont, S., L. Morsut, M. Aragona, E. Enzo, S. Giulitti, M. Cordenonsi, F. Zanconato, J. Le Digabel, M. Forcato, S. Bicciato, N. Elvassore, and S. Piccolo. 2011. Role of YAP/TAZ in mechanotransduction. Nature 474:179-183.
55. Schoenwaelder, S. M., and K. Burridge. 1999. Bidirectional signaling between the cytoskeleton and integrins. Curr Opin Cell Biol 11:274-286.
56. Dupont, S. 2016. Role of YAP/TAZ in cell-matrix adhesion-mediated signalling and mechanotransduction. Exp Cell Res 343:42-53.

754 57. Puklin-Faucher, E., M. Gao, K. Schulten, and V. Vogel. 2006. How the headpiece hinge angle is
755 opened: New insights into the dynamics of integrin activation. J Cell Biol 175:349-360.

756